Photonic-Plasmonic Coupling Enhanced Fluorescence Enabling Digital-Resolution Ultrasensitive Protein Detection

AUTHOR NAMES:

Priyash Barya[‡ 1,2], Yanyu Xiong[‡ 1,2], Skye Shepherd[‡ 3,4], Rohit Gupta[6], Lucas D. Akin[2,5], Joseph Tibbs[3,4], Han Keun Lee[1,2], Srikanth Singamaneni[,7], Brian T. Cunningham[*,1,2,3,4,5,6]*

[‡] These authors contributed equally to this work.

AUTHOR ADDRESS:

[1] Department of Electrical and Computer Engineering, University of Illinois at Urbana−Champaign, Urbana, Illinois, 61801, USA

[2] Holonyak Micro and Nanotechnology Laboratory, University of Illinois at Urbana−Champaign, Urbana, Illinois, 61801, USA

[3] Carl R. Woese Institute for Genomic Biology, University of Illinois at Urbana−Champaign, Urbana, Illinois, 61801, USA

[4] Department of Bioengineering, University of Illinois at Urbana-Champaign, Urbana, Illinois, 61801, USA

[5] Department of Chemistry, University of Illinois at Urbana-Champaign, Urbana, Illinois, 61801, USA

[6] Cancer Center at Illinois, University of Illinois at Urbana-Champaign, Urbana, Illinois, 61801, USA

[7] Department of Mechanical Engineering and Materials Science, Institute of Materials Science and Engineering, Washington University in St. Louis, St. Louis, Missouri 63130, United States

[*] Correspondence to: bcunning@illinois.edu, singamaneni@wustl.edu

KEYWORDS: biosensor, photonics, plasmonics, fluorescence, immunoassay

ABSTRACT

Assays utilizing molecular fluorophores are common throughout life science research and diagnostic testing, although detection limits are generally limited by weak emission intensity, thus requiring many labeled target molecules to combine their output to achieve signal-to-noise greater than the background. Here, we describe how the synergistic coupling of plasmonic and photonic resonance modes can significantly boost the emission from fluorescent dye molecules without increasing the illumination intensity while utilizing a microscopy approach with a broad field of view. By optimally matching the resonant modes of a plasmonic fluor (PF) nanoparticle and a photonic crystal (PC) surface with the absorption and emission spectrum of the PF's fluorescent dye, we observe a 52-fold improvement in signal intensity, enabling individual PFs to be observed and digitally counted, using an approach in which one PF tag represents detection of one target molecule. The photonic amplification from the PF can be attributed to the strong near-field enhancement due to the cavity-induced activation of the PF, PC band structure-mediated improvement in collection efficiency of emitted photons, and increased rate of spontaneous emission. We demonstrate the applicability of the method by dose-response characterization of a sandwich immunoassay for human interleukin-6, a biomarker commonly used to assist diagnosis of cancer, inflammation, sepsis, and autoimmune disease. We achieve a limit of detection of 10 fg/ml, representing a capability three orders of magnitude lower than standard immunoassays.

40 INTRODUCTION

41 Fluorescence-based bioanalytical techniques are among the most predominant methods for
42 quantitative detection of many classes of biomolecules[1-3]. The basic working principle involves
43 attachment of the fluor to a biomolecule with a covalent chemical bond, and with knowledge of
44 the absorption and emission spectra of the fluor, selecting an appropriate illumination source and
45 emission filter to enable observation with a single-element photodiode or an array of photodiodes
46 in an image sensor. Fluorescent dyes are commonly utilized elements within flow cytometers,
47 microscopy, lab-on-a-chip systems, and health diagnostics instruments due to their versatility in
48 terms of selective attachment to other molecules, low cost, wavelength versatility, and ease of use.
49 However, the main limitations for fluorescent dyes in the context of bioassays are rapid
50 photobleaching, and the low number of detectable photons/fluor, as dictated by fluorescent
51 lifetime, collection efficiency, and excitation efficiency. Typically, an efficient photon-collecting
52 high numerical aperture (NA) objective or electron-multiplying charge-coupled device camera is
53 required for imaging single fluorescent tags[2, 4], resulting in expensive instrumentation, that limits
54 their use in point-of-care diagnostic testing and routine life science research. When individual
55 fluorophores are used to label individual target biomolecules in an assay, the limitation manifests
56 itself in the requirement to aggregate many analytes together, so as to combine the output of many
57 fluors. Many emitters are required to enable observation above noise due to the combined effects
58 of background fluorescence from the environment and the inherent noise of the photodetector (dark
59 current and shot noise). Thus, detection of target biomolecules in fluorescent assays on ordinary
60 surfaces, such as glass and plastic, typically achieve detection limits in the 1-100 pg/ml range as
61 observed in array formats in which a capture molecule is applied to an assay surface in the form
62 of a small spot [5-7]. Prior research in the use of resonant dielectric nanostructures, such as photonic

63 crystals (PCs)[8-10], zero-mode waveguides[11, 12], microring resonators[13] and plasmonic surfaces[14, 15]
64 have sought to overcome the inherent brightness limitations of fluorophores through enhancement
65 in the excitation intensity, increased collection efficiency of emitted photons through directional
66 extraction, and reduced lifetime through the Purcell effect.

67 While these approaches have proven effective for reducing detection limits for biosensing
68 assays, the techniques are not capable of reducing limits of detection and quantitation to the
69 ultimate limit of digital resolution, in which each detected molecule may be counted individually[16,
70 17]. While digital resolution biodetection may be achieved through partitioning of the sample into
71 thousands of individual droplets, followed by enzymatic amplification, as with ddPCR[18],
72 BEAMing[19], and Quanterix Simoa™ assays[20], we seek a more direct and simple approach in which
73 a nanoparticle tag is attached to each target molecule, and a simple and inexpensive optical
74 detection instrument counts the tags with high signal-to-noise ratio.

75 Plasmonic nanoparticles and nanoantennas produce near-field fluorescent enhancements
76 due to their small modal volumes[21-23] while also drastically increasing the local density of states
77 (LDOS) near the emitter, thus increasing the rate of spontaneous emission[24, 25]. Recently, by
78 coating a plasmonic nanostructure with fluorophores, stable and ultrabright fluorescent
79 nanoconstructs have been applied as fluorescent reporter tags[26, 27]. However, plasmonic
80 nanostructures are also associated with high losses due to nonradiative processes and lack of
81 directive emission[28, 29]. One approach to mitigate the losses has been coupling the plasmonic
82 nanoantenna to a photonic resonator which could effectively depolarize the antenna, lowering its
83 absorption in a narrow spectral window[30, 31]. Additionally, the resonant matching of these two
84 oscillators can result in an enormous increase in near-field enhancement[26, 32]. Utilizing a dielectric

85 structure like a photonic crystal (PC) could also mitigate the lack of directive emission by enabling
86 controlled Bragg scattering[8, 33].

87 In this work, we describe an approach for achieving digital-resolution detection of target
88 biomolecules through the synergetic interplay of plasmonic and photonic resonances to boost the
89 emission of fluorescent dye molecules. The approach builds upon our recent exploration of
90 plasmonic-photonic hybrid coupling between plasmonic nanoparticles and a PC surface, in which
91 enhanced absorption cross section results from strategic selection of the nanoparticle LSPR
92 wavelength with respect to the PC band structure[30], which we demonstrated as an effective means
93 for enhanced surface-enhanced Raman scattering[32] and electromagnetically enhanced catalysis of
94 chemical reactions[16]. The key benefits the hybrid coupling brings is (1) the strong near-field
95 enhancement which tightly focuses the excitation energy for the absorption by fluorophores, (2)
96 the fluorescence emission couples into PC guided resonances and redirects the photons towards
97 the collection objective for efficient extraction (3) the increased rate of spontaneous emission
98 improves the rate of photon generation. This work also builds upon our recent advances with the
99 design, synthesis, and application of Plasmonic Fluor (PF) nanoparticle tags, in which metallic
100 nanorods are coated with a ~3 nm thick dielectric spacer layer, followed by a coating of molecular
101 fluorophores and target-specific capture molecules[27, 34, 35]. Here, we combine PCs and PFs as a
102 hybrid system for the purpose of using PFs as digital-resolution tags in the context of a surface-
103 based sandwich assay. We experimentally investigate the PC+PF hybrid system by constructing
104 plasmonic nanostructures coated with a layer of fluorescent dyes and record the fluorescence
105 enhancement on a PC substrate. Electromagnetic numerical simulations and a theoretical model of
106 the hybrid enhancement are used to support experimentally measured enhancements, and to
107 describe the design parameters for optimal coupling. We demonstrate the applicability of the

method with the detection of human interluekine-6 (IL-6), a pro-inflammatory cytokine used in the diagnosis of cancer, sepsis, and autoimmune disease. We achieve a limit of detection of 10 fg/ml (representing approximately 20,000 molecules in a 100 µl assay volume) and a 7-log quantitative dynamic range. The PC+PF hybrid system provides a 52-fold signal enhancement compared to detecting PFs on an ordinary glass surface, which facilitates digital counting of PFs with a line-scanning instrument using an inexpensive 0.25 NA objective. The instrument scans a 1.2x1.0 mm^2 sensor area in ~5 minutes, thus overcoming the surface area limitations associated with oil-immersion lenses and resonators such as micro-rings. Our reported detection limit is three orders lower than conventional microplate ELISA and on a similar range to more sophisticated digital microbead approaches like Simoa[36] for the same IL-6 analyte.

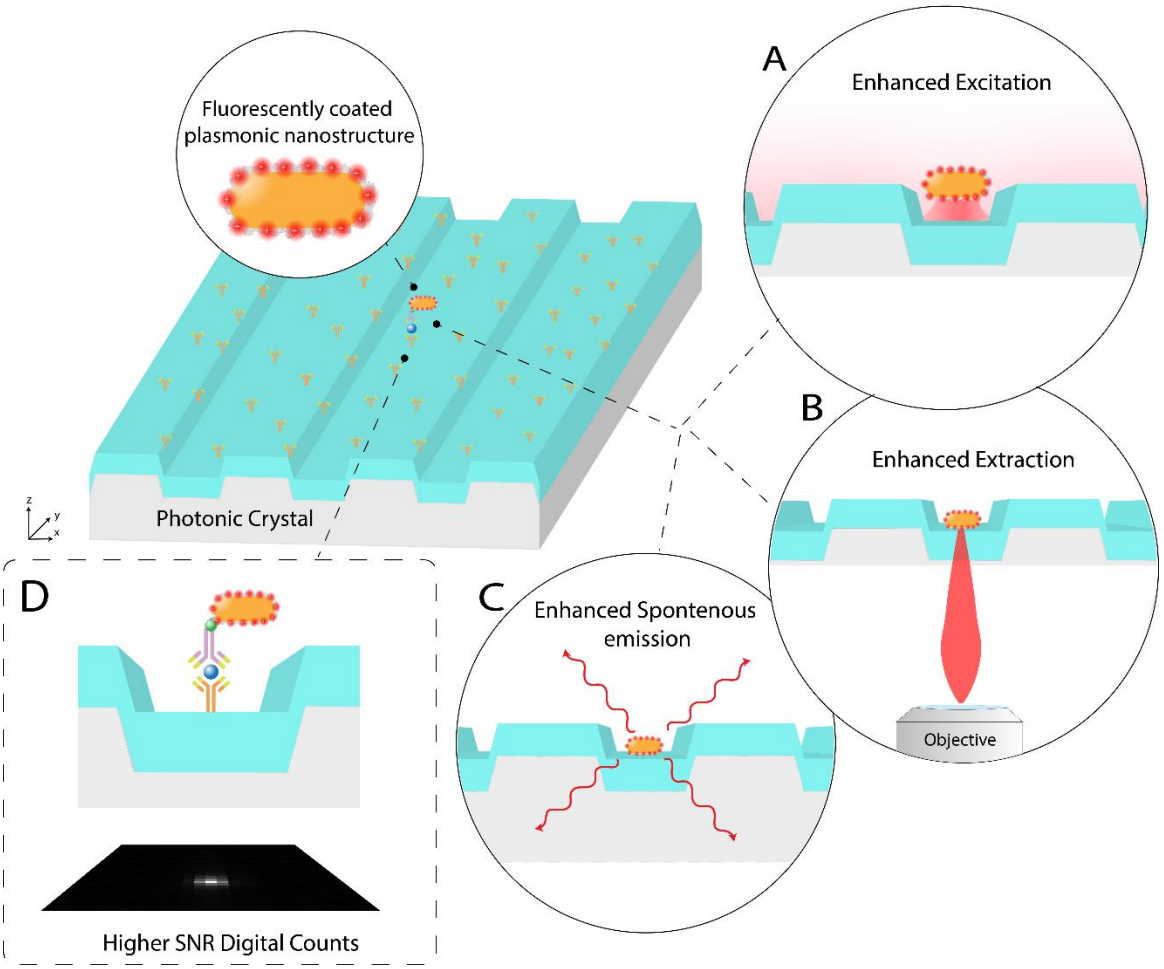

Figure 1. Principle of plasmonic-photonic hybrid for fluorescence enhancement applied towards a digital resolution immunoassay. (a) Enhanced excitation due to near field enhancement (b) Improved extraction efficiency towards a collection objective and (c) Increased rate of spontaneous emission. (d) The sandwich assay design utilized on the PC surface with PFs as fluorescent labelling tags for digital resolution detection.

RESULTS AND DISCUSSION

To exploit the photonic-plasmonic hybrid coupling towards enhancing the fluorescence of an emitter, we recognized key design criteria towards engineering the PC and PF nanostructures. It is critical for the PC band structure to be designed such that there are resonant leaky modes overlapping both the excitation and emission spectra of the chosen fluor[8, 9]. Furthermore, engineering constraints of utilizing an inexpensive lower NA objective (NA = 0.25) dictates the following criteria for the PC: (1) The existence of a resonant mode at the excitation wavelength, which can couple the input laser source at an angle lower than the NA of the objective. (2) Leaky resonant modes overlapping the fluor emission spectrum which out-couple the emitted fluorescence at angles under the angular collection bandwidth of the objective lens. (3) The PF resonance should encompass both the absorption and emission spectrum of the fluor[22] to provide a combined advantage of enhanced near field excitation and an increase in the rate of emission through the Purcell effect.

Note that the three criteria require the PC and PF resonant frequencies (ω_{PC} *and* ω_{NC}) to be strategically matched ($\omega_{PC} \approx \omega_{NC} = \omega_o$). A further less obvious design criteria is: (4) Matching the radiative decay rate of the PC and the non-radiative decay rate of the PF. This can be more closely understood by describing the hybrid system using the temporal coupled mode theory (TCMT) [26, 37]. Let us consider the hybrid coupling between the plasmonic nanostructure and the

PC guided resonance (PCGR) with radiative (γ_r) and non-radiative decay rates (γ_{nr}) . Since the PC is made of low-loss dielectric material, the non-radiative decay is assumed to be dominated by the lossy-metallic nanostructure ($\gamma_{nr} \approx \gamma_{ab}$). We can describe the amplitude of the oscillation (a) as:

$$|a|^2 \propto \frac{1}{(\omega - \omega_o)^2 + (\gamma_r + \gamma_{abs})^2} \quad (1)$$

Using Eqn. 1, we can further evaluate the excitation enhancement at the resonant frequency ($\omega = \omega_o$) [38] (details in Supplemental Note 1)

$$\Lambda_E = \frac{2\, c\, \alpha^{\mathrm{E}}}{n d_{eff}^{E}} \frac{\gamma_r^E}{(\gamma_r^E + \gamma_{abs}^{\mathrm{E}})^2} \qquad (2)$$

Where n is the refractive index of surrounding medium, d_{eff}^{E} is the effective length of the evanescent field, and the α^{E} is the modal field confinement for the excitation mode. While evaluating enhanced extraction, the angular emission of molecules is altered due to the modification of the spectral density of states. Due to Helmholtz reciprocity, the outcoupled emitted photons from the resonator would be dictated by the mode solution obtained in Eqn. 1. By decomposing the Green's function in the normalized Bloch mode basis with a finite resonance lifetime described by Eqn. 1, we can derive the enhanced rate of extraction (Λ_{k}) for a specific (k, ω_k) as (details in Supplemental Note 1):

$$\Lambda_{\mathrm{K}}(k, \omega_k) = \frac{c\, \alpha^{\mathrm{K}}}{\mathrm{n} d_{eff}^{\mathrm{K}}} \frac{\gamma_r^{\mathrm{K}}}{(\gamma_r^{\mathrm{K}} + \gamma_{abs}^{\mathrm{K}})^2} cos\theta_k \quad (3)$$

Where α^{K} is the energy confinement of the resonance mode and d_{eff}^{K} is the effective length of the evanescent field in the molecular layer in the extraction mode of emission. From Eqn. 2-3, we observe that the excitation (Λ_{E}) and extraction (Λ_{K}) enhancement are maximized when the rate of

radiative decay in the PCGR mode is equal to the rate of non-radiative decay of the plasmonic nanostructure ($\gamma_r = \gamma_{nr} = \gamma_{ab}$).

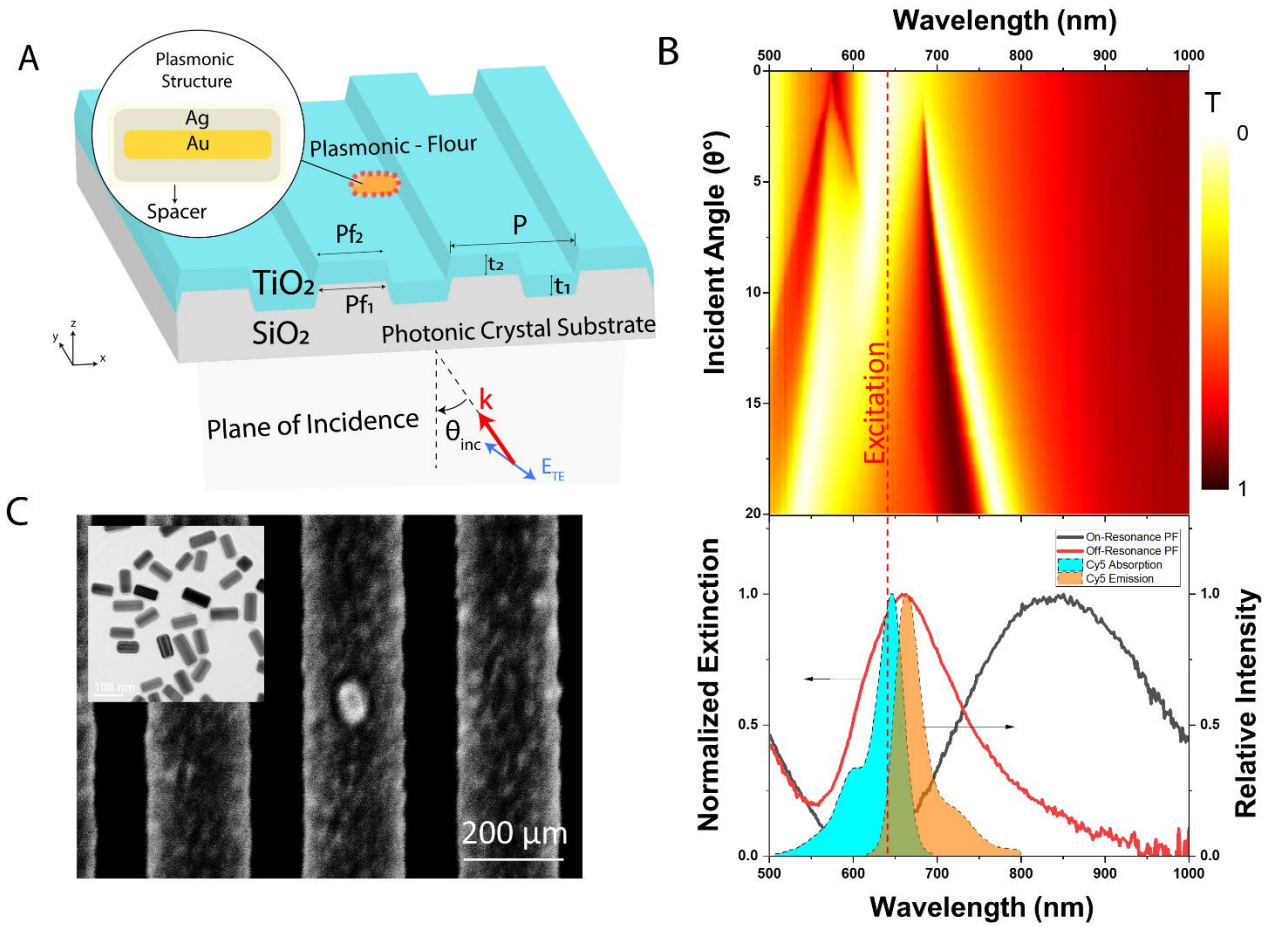

Figure 2. Design of the plasmonic-photonic hybrid for fluorescence enhancement. (a) PF on a PC surface. The structural parameters of the PC are: P = 380 nm, f_1 = 0.34, f_2 = 0.6, t_1 = 80 nm, t_2 = 114 nm. The excitation source is ($\lambda_{ext} = 633$ nm) is TE polarized E field at an incidence angle of θ_{inc} (b) Experimentally measured dispersion diagram from the transmission spectrum with the laser wavelength marked with a dashed red line. Lower panel: Extinction measurements of the on-resonance and off-resonance PFs with similar surface areas. The shaded regions correspond the absorption and emission spectra of Cy5 dye (c) Representative SEM image of a PF on the PC surface. Inset: TEM images of PFs.

173 Based on this theoretical framework and design criteria, we engineered the two nanostructures
174 individually and later integrated them to investigate the enhanced fluorescence. We first
175 synthesized a stable fluorescently labelled PF. Following our third criteria, the PF is comprised of
176 an inner gold nanorod core surrounded by a coating of silver, as shown in the transmission electron
177 microscope (TEM) image in Fig. 2 (c). An additional siloxonane copolymer layer was used to
178 create a spacer layer between the fluor layer and the metal surface. The optimal distance reduces
179 the effect of metal induced fluorescence quenching while remaining in the vicinity of the strong
180 near field. The LSPR of the synthesized particles was evaluated by measuring the extinction of the
181 PFs on a TiO_2-coated glass substrate to mirror the dielectric environment of the PC surface. As
182 shown in Fig. 2(b), the PF exhibits a resonance near 660 nm, encompassing both the absorption
183 and emission spectrum of the coated Cy5 dye.

184 Subsequently, we designed the PC following the requirement of using an inexpensive widefield
185 0.25 NA objective allowing a 15° window for excitation and extraction. The structure is composed
186 of a periodically modulated glass substrate with a film of TiO_2 (n = 2.4) deposited on top (Fig. 2
187 (a)(c)). The band structure was experimentally verified using far-field transmission measurements
188 which shows close correspondence with the simulated band diagram (see Fig. S1). The PC
189 exhibited a resonance at the excitation HeNe laser wavelength (λ_{ext}) of 633 nm at near normal
190 incidence for the transverse electric mode of excitation. Moreover, the radiative decay of this PC
191 mode ($\gamma_{\mathrm{r}} = 7.08 \times 10^{14}\ \mathrm{rads}^{-1}$) was nearly equivalent to the estimated non-radiative decay
192 rate ($\gamma_{\mathrm{ab}} = 7.44 \times 10^{14}\ \mathrm{rads}^{-1}$) of the NP (see Supplemental Note 1), achieving the optimal
193 coupling condition previously derived from Eqn. 2.

194 A diluted concentration of streptavidin-coated PFs were conjugated on top of the PC surface
195 coated with biotinylated-BSA (50 pg/ml) alongside additional BSA blocking to ensure a sparse

density of nanoparticles (~ 10^{-3}/ μm^2) and later dried. To experimentally interrogate the fluorescence enhancement resulting from different resonant modes of excitation, we built an epifluorescence detection instrument which provides precise control over the excitation angle in the *xz*-plane by translating the focused laser line along the back focal plane of a 10X (0.25 NA) objective lens (Fig. S2). The arrangement enabled us to couple the excitation laser through the phase matching condition into the guided resonance mode of the PC. The off-resonance condition was interrogated by tuning the angle of incidence away from the phase matching condition, effectively depriving the system of any guided resonance enhancement from the excitation source. Direct comparison to an unpatterned sample (incapable of enhanced excitation or directional extraction) was performed on a TiO_2-coated glass substrate illuminated at normal incidence. A sample set of 100 individual PFs were imaged and processed to extract their peak fluorescence intensity for each mode of excitation, as shown in Fig. 3 (a).

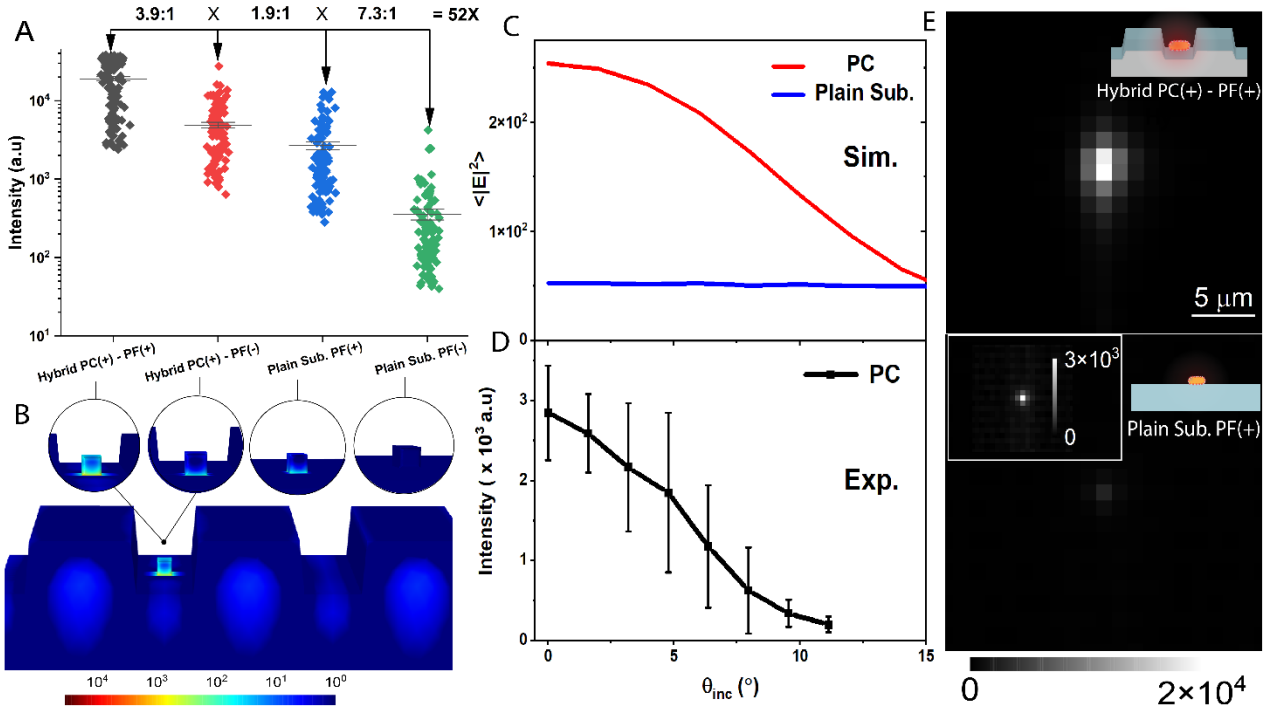

209 **Figure 3**. Fluorescence enhancement due to plasmonic-photonic coupling. (a) and (b) correspond
210 to the experimentally measured peak fluorescence intensity and simulated near-field intensity ($|E|^2$)
211 for on-resonance (Hybrid PC(+) - PF(+) at $\theta_{inc} = 0^o$), off-resonance (Hybrid PC(-) - PF(+) at $\theta_{inc} =$
212 13°) excitation of the PC and on-resonance (Plain Sub. PF(+) at $\theta_{inc} = 0^o$) and off-resonance PF
213 (Plain Sub. PF(-) at $\theta_{inc} = 0^o$) on an unpatterned TiO_2 coated glass substrate respectively. (c) The
214 simulated $<|E|^2>$ near-field intensity for the excitation laser wavelength ($\lambda_{ext} = 633$ nm) at
215 different angles of incidence. (d) Experimentally measured fluorescence intensity of the PF as a
216 function of θ_{inc}. (e) Representative fluorescence image of the PF when the on-resonance condition
217 is engaged (top) and PF on an unpatterned TiO_2 substrate (bottom).

218 We first sought to understand the effect of resonance matching of the plasmonic nanostructure
219 with the absorption and emission spectra of the fluorescent dye. We employed off-resonant
220 nanostructures with nearly the same surface area ($\sigma_{off} = 1325$ nm^2) as the on-resonance particle
221 ($\sigma_{off} = 1206$ nm^2) which would ensure a similar density of fluorophore conjugation on both
222 particles. The off-resonant particle exhibited a resonance at a wavelength of approximately 850
223 nm (Fig. 2 (b)), removing the possibility for surface plasmon resonance mediated enhancement.
224 The peak fluorescence of both particles conjugated on an unpatterned substrate demonstrated 7-
225 fold increase when the resonance condition is satisfied (Fig. 3 (a)). The enhancement is the result
226 of both the increase in the excitation rate due to near field and the increase in the rate of
227 spontaneous emission.

228 To investigate the contribution of Purcell enhancement, we carried out time-resolved
229 photoluminescence measurements in the frequency domain. The average fluorescence lifetime for
230 Cy5 and the on-resonance PF were 1 ns and 0.328 ns respectively (Fig. 4 (d)), resulting in a 2.8-
231 fold increase in quantum efficiency, from 27% to 76% for the on-resonance PF (see Supplementary

Note 3). The remainder of the enhancement can be attributed to the near-field enhancement due to the LSPR resonance. To evaluate the effect, full-wave electromagnetic simulations of the average density of near-field intensity inside the spacer layer $< |E|^2 > \; = \int E^2 \, dr^3 / \int dr^3$ showed a 10.9-fold increase when the plasmon resonance is closely matched to the fluor's peak excitation wavelength (Fig. S4). Experimental measurements reveal a lower enhancement than the theoretically predicted value, which can be attributed to fluorescence quenching due its proximity with a lossy metallic surface. The field enhancement inside the spacer layer can be further amplified through the hybrid integration of the plasmonic nanostructure with a resonantly excited PC.

The contributions of near-field enhancement due to the hybrid coupling can be understood by observing the angle-dependent resonance excitation of the PC. We observe that during the on-resonance excitation (θ_{inc} = 0°), the average fluorescence was 3.9-fold higher than the off-resonance (θ_{inc} = 13°) excitation (Fig. 3 (a)). This is the consequence of the PCGR mode coupling the excitation energy into a guided resonance and feeding the PF through a strong near-field interaction. The resonant coupling improves the efficiency with which the PF interacts with the input excitation. As a result, the surrounding spacer layer consisting of fluorescent dyes experiences an increased excitation energy. For further validation through numerical simulations, $<|E|^2>$ was evaluated for the hybrid coupled resonance, and a solitary nanoantenna on an unpatterned TiO_2 substrate for the TE mode of excitation. The increase in the field intensity ($\lambda_{ext} = 633$ nm) around the nanorod can be observed when the phase matching condition with the incident wave excites the PCGR mode, whereas the value is angle-insensitive for the TiO_2 substrate (Fig. 3 (c-d)). As a result, the PF tightly concentrates the field intensity with a maximum enhancement of over 10^4 in certain regions of the spacer layer (Fig. 3 (b)). On comparison with

255 the same nanostructure on an unpatterned TiO_2 substrate, the simulated $<|E|^2>$ was 4.8-fold higher
256 on the PC surface (Fig. 3 (c)), which is in good agreement with our experimentally obtained near-
257 field enhancement (Fig. 3 (a)).

258 It is noteworthy that the broadened signal distribution observed in Fig. 3 (a) and Fig. 3 (d) can
259 be attributed to two phenomena: (1) Variation of near-field intensity along the PC surface, resulting
260 in a variability in the excitation energy depending on the relative position of the PF. (2)
261 Polarization sensitive enhancement due to relative orientation of the PF with respect to the PC
262 grating direction (see Fig. S5). One strategy to overcome these problems is the utilization of a 2D
263 PC lattice design that could potentially provide a more uniform field distribution if two guided
264 resonance modes are engineered to interact[39]. Moreover, the isotropic nature of a PC with 2D
265 symmetry would eliminate the requirement of polarized excitation and reduce the effect of
266 orientation-induced broadening of the intensities. Another strategy to minimize the effect of
267 polarization sensitivity could be the utilization of a PF with more spherical symmetry, such as
268 nano-cuboids that satisfy the same LSPR selection criteria as nanorods[40].

269 We next investigated the far-field properties of the PC+PF hybrid system by characterizing the
270 effects of directional emission extraction. On comparing the off-resonance fluorescence on the PC
271 with the intensity measured from PFs on an unpatterned TiO_2-coated glass substrate, we observed
272 a 1.8X higher signal (Fig. 3 (a)), attributed to the coupling of the fluorescence emission with the
273 leaky-PCGR modes which redirect the photons according to bandstructure as described in prior
274 research[8, 16]. As a result, the angular emission for the dye follows the isofrequency contours of the
275 PC, as described by the allowed resonance solution of the PC in momentum space (k_x, k_y) at a
276 constant frequency ω.

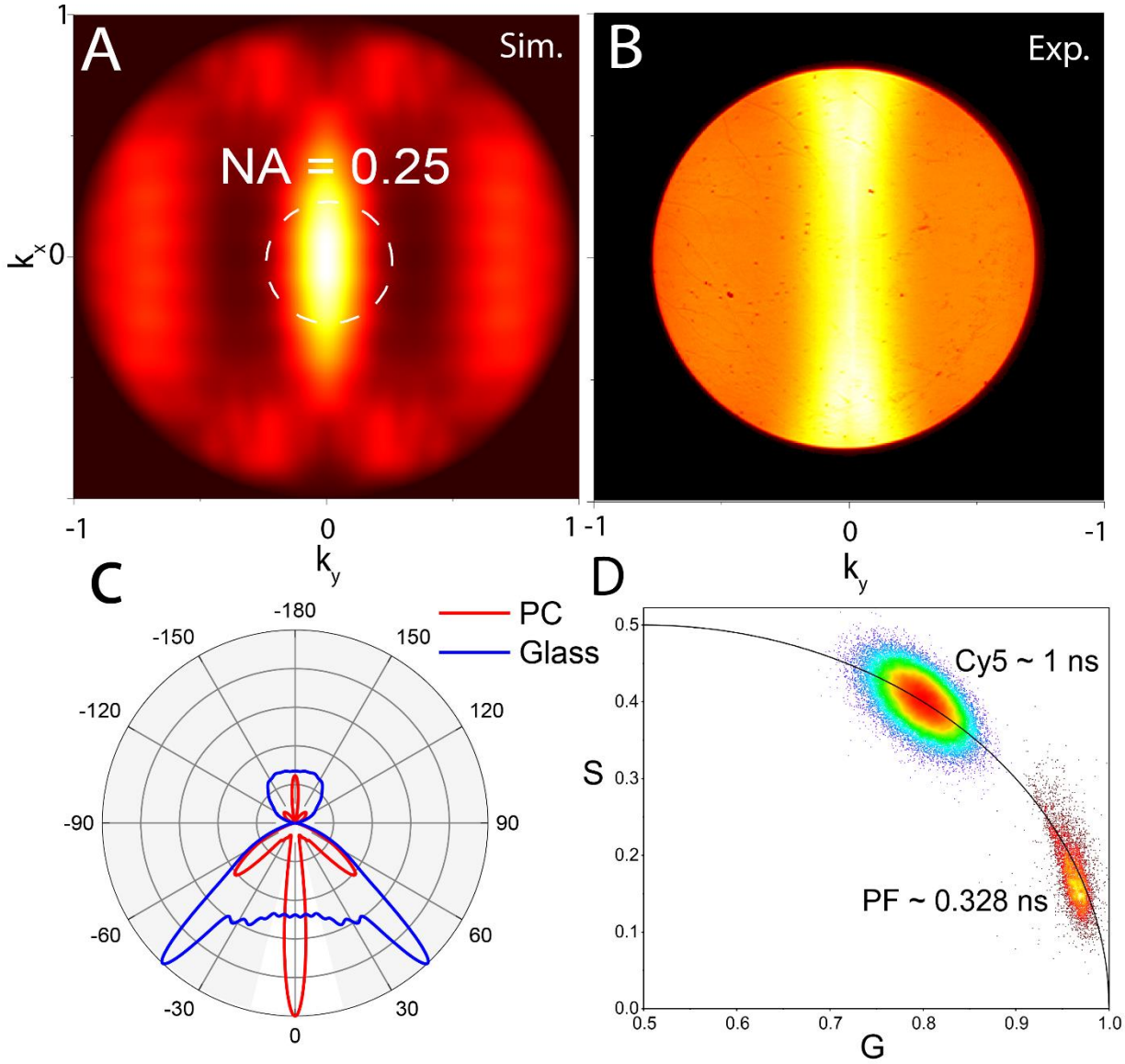

Figure 4. Enhancement due to extraction and the Purcell effect (a) Simulated Fourier plane image of PF on the PC surface (b) Experimentally measured back focal plane images of the PF in the TE mode of excitation (c) Simulated far-field radiation pattern of the PF on a PC and glass substrate. The white opening represents the allowed angular window for NA = 0.25 (d) Experimentally obtained phasor plot comparing the estimated lifetime of the Cy5 molecule and the PF.

284 In order to experimentally explore the k-space information of the emitted fluorescence, we
285 imaged the back focal plane of the collection objective. We observe that the PC redirects the
286 photons towards the normal axis of the collection objective, providing a more efficient pathway
287 for collecting the emitted photons (Fig. 4 (b)). We further validated the experimental data with
288 FDTD simulations to calculate the far-field radiation pattern and the collection efficiency (CE) for
289 a PF on the PC. The modelling was performed by assuming a dipole source placed between the
290 NP and the PC surface. The electric field was recorded below the lower grating and projected to
291 the far-field to obtain ($E(k_x, k_y)$) The simulated data Fourier plane showed a good correlation
292 with the experimental BFP (Fig. 4 (a-b)) and the 2D far-field radiation pattern (at $I(k_x = 0, k_y)$)
293 elucidates the difference between glass and PC surfaces (Fig. 4 (c)). The unpatterned surface has
294 its major lobes near 45°, close to the critical angle of the glass/air interface. As a result, a large
295 proportion of photons will be lost due to the reflection at this interface, resulting in poor collection
296 efficiency for air-based objective. On the other hand, the PC band structure minimizes this effect
297 by redirecting the photons towards the normal axis of the collection objective (Fig. 4 (c)). We
298 further numerically calculated the CE as the ratio between collected power by the microscope
299 objective (S_{col}) and the total emitted power (S_{tot}) by the fluorescent molecule ($CE = \frac{S_{col}}{S_{tot}}$). On
300 comparing the two substrates at the peak fluorescence emission ($\lambda_{em} = 665$ nm), we estimate a
301 2X improvement in CE, correlating well with the experimentally obtained increase in fluorescence
302 intensity (see details in Supplementary Note 3).

303 **Digital Resolution Bioassay**

304 Of the numerous applications possible due to the hybrid enhancement, we demonstrate a digital
305 resolution sandwich assay for the cytokine protein human Interleukin-6 (IL-6). IL-6 was selected
306 for both its clinical utility as a diagnostic test for inflammation-related health conditions, and

307 because it is a target biomolecule utilized in nearly all other detection technologies for performance
308 benchmarking. The conventional enzyme/fluorescence-linked immunosorbent assay
309 (ELISA/FLISA) utilizes a polystyrene microtiter plate with a capture antibody, biotinylated
310 detection antibody, target analyte (Human IL-6) which is followed by exposure to an enzyme-
311 substrate or streptavidin-fluorophore. In our method, the imaging substrate is replaced with a PC,
312 while PFs are utilized as tags for the same assay design (Fig. 5 (a)). To efficiently conjugate capture
313 antibodies, the TiO_x groups comprising the PC surface were chemically modified. Oxygen plasma
314 activated PCs were silanized to achieve isocyanate functionality that facilitate antibody
315 conjugation by reacting with the amine groups of lysine side chains. The corresponding urea
316 linkage formed by this mechanism is stable at room temperature and resistant to further hydrolysis.
317 Isocyanate groups that do not undergo rapid conjugation are efficiently converted to their
318 corresponding amine via nucleophilic attack from surrounding water molecules, which promotes
319 release of carbon dioxide. In order to maximize antibody immobilization density, we employed
320 disuccinimidyl carbonate (DSC)[41] as a secondary reaction component, which allowed for the
321 regeneration of reactive isocyanates and succinimidyl carbamates that mutually facilitate
322 immobilization via formation of a urea linkage between the antibody and the PC surface (see Fig.
323 S6).

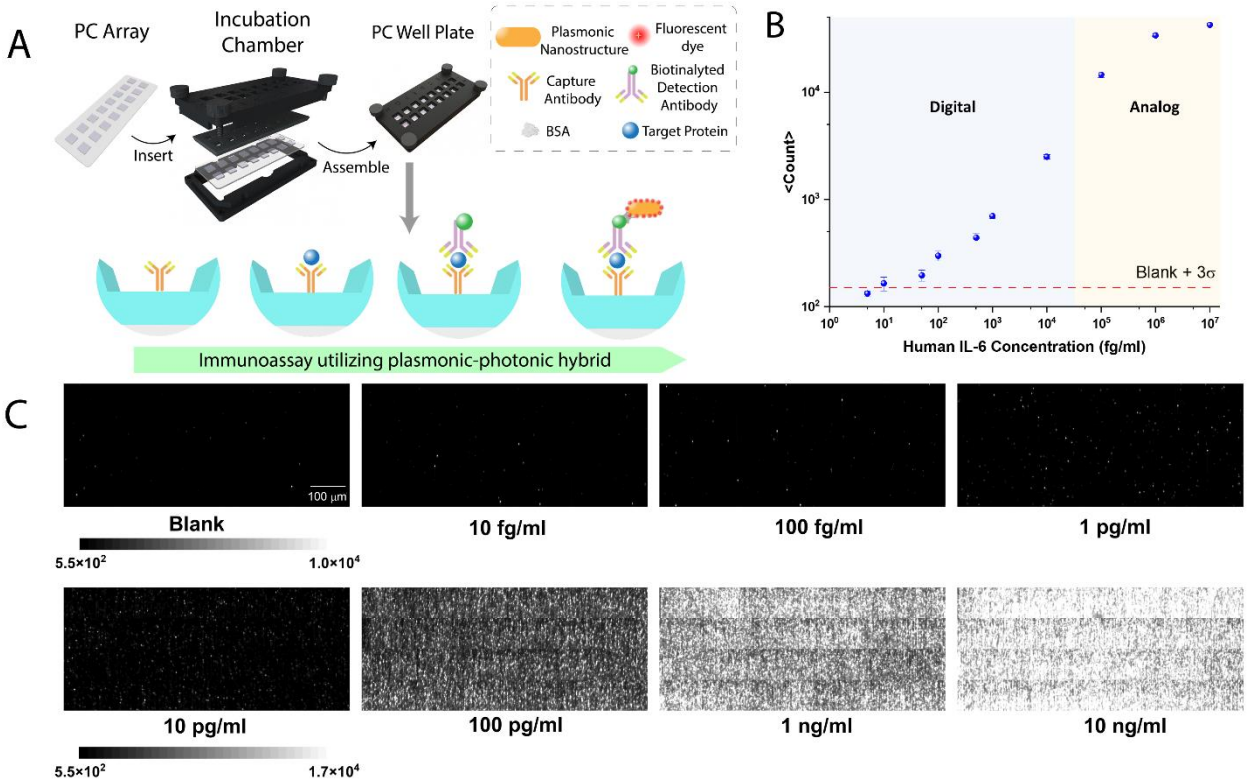

Figure 5. Digital resolution protein detection assay for IL-6 (a) Schematic illustration of the PF based immunoassay performed on a PC integrated within a multi-well plate. (b) Digital counts of the IL-6 immunoassay at different analyte concentrations. Blue region indicates the concentrations the algorithm utilized a digital counting method, and the orange area describes the region the analog intensity of fluorescent spot was used to estimate the digital count (3 repeats). (c) Representative fluorescence grey -scale images of a sub-area (0.4x1 mm^2) showcasing the digital resolution PFs as a function of IL-6 concentration

To gauge the improvements in the sensitivity and the limit of detection, serial dilutions of IL-6 (10 ng ml^{-1} to 5 fg ml^{-1}) were spiked into a PBS buffer solution to generate a dose-response standard curve. The assay was performed by incubating the 100 µl test sample upon the PC surface at room temperature for 2 hours, followed by a washing step with PBST buffer. A solution of 50

337 ng/ml biotinylated anti-IL6 were incubated on the PC surface for 2 hours, followed by a second
338 washing step. Subsequently a solution of $2x10^7$ particles/ml streptavidin coated PFs were
339 incubated for 30 minutes followed by a final washing step. A 1.2 x 1.0 mm^2 area of the PC was
340 scanned by tiling together 300 x 4.5 μm^2 sub-images, and the appended images were processed to
341 digitally count individual PFs (Fig. 5 (c)). Each sub-area scan required 100 msec, and the entire
342 imaged area of 900 tiles required a scanning time of 5 minutes. The PFs are easily distinguished
343 as individual units, where their signal-to-noise ratio (compared to the dark background of the non-
344 fluorescent regions) is ~55:1, highlighting the advantage of utilizing the PC+PF hybrid system to
345 enhance the signal. We obtained a Limit of Detection (LOD) of 10 fg/ml, which was calculated
346 by determining the concentration of target analyte with a digital count equal to 3 times the standard
347 deviation above the mean of the blank control concentration (Fig. 5 (b)). The LOD represents six
348 orders lower than the reported for conventional FLISA and three orders lower than reported for
349 conventional ELISA[34]. We also note that the detection limit achieved is 500x lower than the 2
350 pg/ml LOD reported for the Luminex flow cytometer-based BeadArray™ technology[42] and similar
351 to the 4 fg/ml reported for the Quanterix Simoa™ technology[36] that requires a much more
352 complicated workflow that involves droplet partitioning, magnetic bead capture, and enzymatic
353 amplification. Importantly, quantitation is maintained over a 7-log dynamic range, up to 10 ng/ml.
354 Digital counting of PFs is utilized for the lowest (and most challenging) concentrations, up to a
355 concentration of ~10^4 fg/ml. As expected, elevated concentrations result in a high density of
356 captured IL-6 molecules, and thus a high density of PFs in the image. Thus, at elevated
357 concentrations, the point spread functions of PFs in the image begin to overlap, and digital
358 counting becomes less effective. However, quantitation can continue to higher concentrations by
359 simply utilizing the "analog" average fluorescence intensity of the image, thus extending the

360 dynamic range by a further 3-logs beyond the digital range. We note that this approach is much
361 simpler and more direct than methods based upon making estimates of biomarker concentration
362 using Poisson statistics and Average Enzymes per Bead (AEB) methodology[43]. It is interesting
363 to note that the LOD of 10 fg/ml represents only ~2.1 x 10^4 molecules in the 100 µl assay volume,
364 and that even with zero flow rate, our 120 minute stagnant incubation time measured 0.15% of the
365 available molecules, assuming 100% efficiency for labeling the captured IL-6 molecules with a
366 PF. Thus, we expect to achieve further reductions in LOD through liquid handling methods (such
367 as stirring) that can help overcome diffusion-based molecular capture limitations.

368 A key advantage of the assay approach that the increased sensitivity does not entail any change
369 in standard assay protocols. As a result, the method can be easily adopted toward a wide variety
370 of biomarkers using sandwich-style assays (as shown here) for detection of proteins, or for
371 detection of nucleic acid analytes (such as specific sequences of mRNA, miRNA, and ctDNA).
372 Moreover, the platform is capable of digital resolution multiplexing in a single test region by
373 utilizing PF tags that incorporate distinctly detectable fluorescence dyes for each analyte, while
374 the PC can be prepared with an unpatterned mixed surface of capture molecules.

375 In summary, to overcome the limitation of weak fluorescence emission, we exploited the
376 synergistic coupling between plasmonic and photonic crystal resonators to amplify the emission
377 intensity of PFs by 52-fold. Through experimentation and numerical simulation, we attribute this
378 increase to the strong near-field enhancement, improved extraction efficiency and boosted
379 quantum yield. We harnessed the amplified intensity towards improving the signal-to-noise ratio
380 of digital resolution immunoassays. By utilizing the plasmonic structures as a fluorescent reporter,
381 integrated with photonic crystals as a readout platform, we obtained a limit of detection of 10 fg/ml
382 for human IL-6. The signal enhancement elucidated here can be easily exploited to improve

383 numerous existing bioanalytical techniques by enabling single-molecule level sensitivity while
384 maintaining cost-effective instrumentation.

385 METHODS

386 **PC Fabrication** - The PC utilized in this work constituted a low refractive index grating coated
387 with a higher refractive index (TiO_2). The structure was fabricated on a glass wafer coated with a
388 10 nm etch stop layer of Al_2O_3. A subsequent SiO_2 layer was deposited, and the periodic grating
389 pattern was constructed by ultraviolet interference lithography carried out by Moxtek (Orem,
390 USA). A TiO_2 layer (thickness ~ 114 nm) was then deposited on the etched wafer using sputtering
391 to create guided waveguide structure.

392 **PF synthesis** - Silver cuboids (AuNRAg) (synthesis in Supplement Note 2) were employed as
393 the plasmonic core to prepare PF. 1 µl of (3-mercaptopropyl)trimethoxysilane (MPTMS) (Sigma
394 Aldrich, 175617) and 1 ml of AuNRAg (extinction ~2) were mixed and shaken on rocking bed for
395 1 hour. Next, 2 µl of APTMS (Sigma Aldrich, 281778) and 2 µl of trimethoxy(propyl)silane
396 (TMPS) (Sigma Aldrich, 662275) was added to the MPTMS-modified AuNRAg to form the
397 polymer spacer layer. Excess monomers were removed from the AuNRAg–polymer solution by
398 two centrifugations at 6000 rpm for 10 min. After each wash the pellet was redispersed in 1 M
399 CTAC aqueous solution to ensure colloidal stability. Polymer coated AuNRAgs were concentrated
400 into a final volume of 5 µl. Next, to conjugate Cy5-BSA-Biotin complex (synthesis in
401 Supplementary Note 2) to polymer modified AuNRAgs, we followed procedures mentioned in
402 previously reported study[44]. Briefly, to allow coating of Cy5-BSA-Biotin to AuNRAgs, the pH of
403 100 µl 4 mg ml^{-1} Cy5-BSA-Biotin was lowered by adding 1 µl of 20 mg ml^{-1} citric acid (Alfa
404 Aesar, 36664). To this solution, concentrated AuNRAg-polymer solution was added, and the
405 resulting solution was sonicated for 20 min in dark. After coating, excess Cy5-BSA-Biotin was

406 removed by centrifugation at 3,000 rpm for 10 min and incubated with 0.4 mg ml^{-1} of Cy5-BSA-
407 Biotin in pH 10 nanopure water (1 µl NaOH in 10 ml of water) for 3 days at 4 °C. Finally, the
408 nanostructures were washed 4 times using pH 10 nanopure water by centrifugation at 3,000 rpm
409 for 10 mins. The nanolabels were then redispersed in 1% BSA in 1X PBS solution for use in
410 immunoassays. To further label streptavidin onto these nanolabels, the biotinylated plasmonic-
411 fluor solution was incubated in 100 µg/ml solution of streptavidin for an hour on the rocking bad
412 and subsequently purified by washing 4 times using pH 10 nanopure water by centrifugation at
413 3,000 rpm for 10 mins.

414 **Spectroscopic measurements** – For the PC transmission band diagram, the sample was
415 mounted on a fine-resolution motorized rotation stage. A deuterium and halogen lamp (Ocean
416 Insight DH-2000-BAL) was used to produce a white light collimated beam of 5 mm^2 area with TE
417 polarization. The incident angle was tuned with computer controlled motorized rotation stage
418 between θ_{inc} = 0°-14°. The zero-order transmission was collected by a fiber collimating lens and
419 guided to a spectrometer (Ocean Optics USB 2000) to measure the spectral intensity.

420 The LSPR measurements of the PF samples were carried out by drop casting them on a TiO_2
421 coated glass slide to mimic the dielectric environment of the PC surface. The extinction spectrum
422 mas measured using a micro spectrometer setup built on a Zeiss Axio Obsever D1 inverted
423 microscope. A sparse density region of the sample was identified, and the transmitted intensity
424 was collected 20X objective lens and directed to a silicon PDA spectrometer.

425 **Numerical simulations** - To simulate the near-field properties, we carried out finite-element-
426 method simulations (COMSOL Multiphysics). The unit cell of the simulation spanned three PC
427 periods (1.14 um) in the *x*-direction and 800 nm in the *y*-direction. The geometric parameters were
428 inferred from atomic force microscope (AFM) measurements and by further best-fitting with the

429 far-field transmission spectra of the bare PC. The refractive index of TiO_2 (n = 2.44) was taken
430 from Seifke[45] and the SiO_2 (n = 1.44) were referred from the manufacturer. The plasmonic
431 nanostructures were extracted from the TEM images and the optical constants of gold and silver
432 taken from Johnson and Christy. $<|E|^2>$ was evaluated in a 2 nm spacer layer with a refractive
433 index of 1.5. The full field solutions of the PC were first calculated assuming Floquet periodic
434 boundary conditions. The field distribution was subsequently used as a background field for the
435 nanoparticle excitation with the Floquet boundary condition replaced with perfectly matched
436 layers.

437 The far-field properties were simulated using finite difference time domain method (Lumerical
438 FDTD). The Fourier plane field distribution was calculated by assuming a monochromatic dipole
439 source placed in a 2 nm gap between the plasmonic flour and the photonic crystal surface. The unit
440 cell consisted of 50 periods, modelling the coupled emission to traverse along the waveguide for
441 a finite lifetime. The structure was surrounded with perfectly matched layers and electric field
442 above and below the plane of the PC were recorded. The field profile was projected from the near-
443 field to the far-field to obtain the k-space intensity ($I(k_x, k_y, \lambda)$) information and was further
444 averaged over the fluorescence emission spectrum of the Cy5 to obtain $I(k_x, k_y)$. The collection
445 efficiency was further calculated as a ratio of the integrated power per unit solid angle across the
446 angular bandwidth of the collection objective and the total solid angle. Furthermore, to account
447 for the losses encountered by the glass/air interface, the Fresnel coefficient was applied to the field
448 distribution (See supplementary note 3).

449 **Imaging setup** – The setup was custom built line-focused epifluorescence microscope setup
450 with a 10X objective (0.25 NA, Olympus LMPLFLN) used for both the excitation and collecting
451 emitted light (see Fig. S2). A red excitation HeNe laser (λ_{exc}= 633 nm) was beam expanded to ~1

452 cm by a two-lens relay. It was subsequently linearly polarized to the transverse electric mode and
453 a half-waveplate provided control over the illumination power. A cylindrical lens focused the beam
454 to the back focal plane of the objective lens which resulted in a focused beam along *xz*-plane and
455 collimated excitation along the *yz*-plane of the sample. A motorized translational stage allowed us
456 to tune the angle of excitation by shifting the position of the focused line beam on the back focal
457 plane. The emitted fluorescence was collection by the objective and an emission notch filter was
458 used to reduce the background laser excitation. A tube lens focused the image plane onto a CCD
459 camera (Synapse EMCCD) which recorded the images. The laser was focused to a line of the area
460 300 µm x 4.545 µm area. A series of images were acquired by translating sample in the *xy*-plane
461 in steps of the focused area resulting in an appended field of view of 1.2 mm x 1 mm.

462 **Image analysis** – The raw images were first Wiener filtered to reduce the non-uniformity
463 appending created by the line scanning. The maximally stable extremal regions (MSER) were
464 adopted for the blob detection algorithm which were binarized above the noise levels of the image.
465 The morphological property and size were used as a selection criterion to determine the count and
466 gauge on the peak, total and average intensity values (see Fig. S3). The signal-to-noise
467 comparisons in the fluorescence enhancement were done by subtracting the background noise
468 intensity of the unconjugated plain substrates with the focused laser ($SNR = \frac{I_{PF} - I_{bg}}{\sigma_{bg}}$).

469 **Lifetime measurements** - The lifetime data in this study were measured using digital frequency
470 domain fluorescence lifetime imaging microscope (FastFLIM, ISS) and analysis with phasor plots.
471 The time-resolved photoluminescence (TRPL) was measured from single PFs or homogeneously
472 distributed dye layer. Using Digital Frequency Domain (DFD) technique allows for the acquisition
473 of Time-Tagged-Time-Resolved (TTTR) data without the dead time typical of Time-correlated
474 single-photon counting (TCSPC) approach. The excitation source was a pulsed single photon laser

475 with single-mode fiber optic output and optical parametric oscillator, producing 100-120 fs pulses
476 at λ_{laser} = 635 nm and a repetition rate of 80 MHz. The emission was collected a high-NA objective
477 lens (NA=1.46, oil immersion, 100X, Zeiss α Plan-APO-CHROMAT) and passed through a band-
478 pass filter (692nm CWL, 40nm Bandwidth) to remove the excitation laser and imaged onto silicon
479 single-photon avalanche photodiodes (Si-SP-APDs). 692nm CWL, 25mm Dia, 40nm Bandwidth.
480 The Single-photon avalanche diodes (SPADs) were connected to a photon counting module to
481 acquire the Time-Tagged-Time-Resolved (TTTR) data to generate the histogram of photon arrival
482 times. The raw FLIM measurements from each pixel are directly located on a 2D phasor plot
483 (Figure 4 (d)). This relationship is represented as a semicircle curve centering at (G=0.5, S=0) with
484 a radius of 0.5 on the phasor plot. The semicircle curve indicates the lifetime trajectory with
485 decreasing lifetime from left to right, where (1, 0) indicates lifetimes near zero to (0, 0) being
486 infinite lifetime.

487 **Surface functionalization** - A Human IL-6 DuoSet ELISA kit (R&D, catalogue number
488 DY206, lot P173353) was used to test PF capture on PCs. The PCs were diced into 3 by 4 mm
489 chips and glued onto coverslips using Norland Optical Adhesive 63 (Thorlabs), with UV curing
490 for 3 minutes. The PC surface was first washed by sonication in acetone, isopropyl alcohol, and
491 MilliQ water for two minutes each, then dried at 120°C for ten minutes. The surface was oxygen
492 plasma-treated for 10 minutes at 100% power in a PicoDiener system, and silanized with a 5%
493 silane mixture (95:5 ratio of 3-(triethoxysilyl)propyl-isocyanate to chlorobutyldimethyl silane,
494 from Millipore Sigma in tetrahydrofuran for 30 minutes at room temperature. The surface was
495 washed again by sonication in acetone, ethanol, and MilliQ water, and wells were added using
496 ProChamber Mircoarray system.

Sandwich ELISA for Human IL-6 Detection - Capture antibodies were added from the DuoSet kit at a concentration of 2 µg/mL in 1xPBS, 100 nM N,N'-disuccinimidyl carbonate for 2 hours at room temperature. The surface was washed five times with PBST, followed by blocking with 200 µl of reagent diluent (1xPBS containing 3% BSA, filtered by 0.2 µm). Washing five times with PBST was repeated, and 100 µl of serially diluted standard solution (tenfold dilution from 1 fg/ml to 10 ng/ml using reagent diluent) were added into the wells and incubated for 2 hours at room temperature. Washing with PBST was repeated after standard human IL-6 incubation, then 200 µl of biotinylated detection antibodies (50 ng/ml in reagent diluent) were incubated for 2 hours. The PCs were washed again and incubated with a $2x10^7$ particles/ml concentration of Cy5-plasmonic fluors in reagent diluent for 30 minutes. A final washing step is repeated, then 200 µl of 1xPBS were added to each well until imaging.

ASSOCIATED CONTENT

Supplementary information

The supporting information file is available free of charge – Supplemental_Information.pdf

Supplementary information includes – Simulation of PC band diagram; schematic of optical setup; image processing and counting algorithm; simulation of the plasmon resonance; variation of the electric field density along the grating; surface functionalization chemistry; derivation of the theoretical framework; detailed synthesis of the PF; collection efficiency and quantum yield calculation; optimization steps for surface conjugation of antibodies.

AUTHOR INFORMATION

Corresponding Author

Brian T. Cunningham – Department of Electrical and Computer Engineering, Department of Bioengineering, Holonyak Micro and Nanotechnology Laboratory, Carl R. Woese Institute for Genomic Biology, Department of Chemistry, Cancer Center at Illinois, University of Illinois at Urbana-Champaign, Urbana, Illinois, 61801, USA; Email - bcunning@illinois.edu

Srikanth Singamaneni – Department of Mechanical Engineering and Materials Science, Institute of Materials Science and Engineering, Washington University in St. Louis, St. Louis, Missouri 63130, United States; Email - singamaneni@wustl.edu

Notes

The authors declare the following competing financial interest(s): S. Singamaneni is an inventor on a pending patent related to plasmonic-fluor technology and the technology has been licensed by the Office of Technology Management at Washington University in St. Louis to Auragent Bioscience LLC. S. Singamaneni is a co-founder/shareholder of Auragent Bioscience LLC. S. Singamaneni along with Washington University may have financial gain through Auragent Bioscience, LLC through this licensing agreement. These potential conflicts of interest have been disclosed and are being managed by Washington University in St. Louis.

Author Contributions

B.T.C., S. Singamaneni, Y.X. and P.B. designed the study. P.B. and Y.X. carried out the optical characterization experiments for the enhanced fluorescence. P.B. performed the numerical simulations and outlined the theory with assistance from Y.X.. S. Shepherd. and P.B. optimized the surface chemistry. S. Shepherd., P.B., R.G., and Y.X. ran the protein detection experiments. R.G. synthesized and characterized the plasmonic-flour particles. Y.X. conducted the BFP

543 enhanced extraction experiments and Purcell factor experiments. L.A., J.T., Y.X., and H.K.L.
544 helped in key steps while designing the PC well plate and bioassay experiments. P.B. drafted the
545 manuscript with the assistance of all the authors.

546 ACKNOWLEDGEMENT

547 The work was supported by National Science Foundation (1900277), National Institute of Health
548 (NIH R01 5R01CA227699-03), and Cancer Center at Illinois (CCIL). Y.X is grateful for the
549 C*STAR fellowship from CCIL and J.T acknowledges support from the NSF graduate fellowship
550 program. The authors also acknowledge Nantao Li, Congnyu Che, Glenn. A. Fried, Leyang Liu,
551 Pin Ren, Shengyan Liu, Hanwei Wang, and Qinglan Huang at the University of Illinois at Urbana
552 Champaign and Yuansheng Sun at the ISS inc. for their valuable discussions.

553 REFERENCES

554 1. Nasu, Y.; Shen, Y.; Kramer, L.; Campbell, R. E., Structure- and mechanism-guided design
555 of single fluorescent protein-based biosensors. *Nat Chem Biol* **2021,** *17* (5), 509-518.

556 2. Ma, F.; Li, Y.; Tang, B.; Zhang, C. Y., Fluorescent Biosensors Based on Single-Molecule
557 Counting. *Accounts Chem Res* **2016,** *49* (9), 1722-1730.

558 3. Hu, J.; Wang, Z. Y.; Li, C. C.; Zhang, C. Y., Advances in single quantum dot-based
559 nanosensors. *Chem Commun* **2017,** *53* (100), 13284-13295.

560 4. Walt, D. R., Optical Methods for Single Molecule Detection and Analysis. *Anal Chem*
561 **2013,** *85* (3), 1258-1263.

562 5. Westermann, D.; Neumann, J. T.; Sorensen, N. A.; Blankenberg, S., High-sensitivity
563 assays for troponin in patients with cardiac disease. *Nat Rev Cardiol* **2017,** *14* (8), 472-483.

564 6. Cohen, L.; Walt, D. R., Highly Sensitive and Multiplexed Protein Measurements. *Chem*
565 *Rev* **2019,** *119* (1), 293-321.

566 7. Seurynck-Servoss, S. L.; White, A. M.; Baird, C. L.; Rodland, K. D.; Zangar, R. C.,
567 Evaluation of surface chemistries for antibody microarrays. *Anal Biochem* **2007,** *371* (1), 105-115.

568 8. Ganesh, N.; Zhang, W.; Mathias, P. C.; Chow, E.; Soares, J. A. N. T.; Malyarchuk, V.;
569 Smith, A. D.; Cunningham, B. T., Enhanced fluorescence emission from quantum dots on a
570 photonic crystal surface. *Nat Nanotechnol* **2007,** *2* (8), 515-520.

571 9. Ganesh, N.; Block, I. D.; Mathias, P. C.; Zhang, W.; Chow, E.; Malyarchuk, V.;
572 Cunningham, B. T., Leaky-mode assisted fluorescence extraction: application to fluorescence
573 enhancement biosensors. *Opt Express* **2008,** *16* (26), 21626-21640.

574 10. Mathias, P. C.; Ganesh, N.; Cunningham, B. T., Application of Photonic Crystal Enhanced
575 Fluorescence to a Cytokine Immunoassay. *Anal Chem* **2008,** *80* (23), 9013-9020.

576 11. Levene, M. J.; Korlach, J.; Turner, S. W.; Foquet, M.; Craighead, H. G.; Webb, W. W.,
577 Zero-mode waveguides for single-molecule analysis at high concentrations. *Science* **2003,** *299*
578 (5607), 682-686.

579 12. Zhu, P.; Craighead, H. G., Zero-Mode Waveguides for Single-Molecule Analysis. *Annu*
580 *Rev Biophys* **2012,** *41*, 269-293.

581 13. Taitt, C. R.; Anderson, G. P.; Ligler, F. S., Evanescent wave fluorescence biosensors:
582 Advances of the last decade. *Biosens Bioelectron* **2016,** *76*, 103-112.

583 14. Santos, G. M.; Zhao, F. S.; Zeng, J. B.; Li, M.; Shih, W. C., Label-free, zeptomole cancer
584 biomarker detection by surface-enhanced fluorescence on nanoporous gold disk plasmonic
585 nanoparticles. *J Biophotonics* **2015,** *8* (10), 855-863.

586 15. Deng, W.; Goldys, E. M., Plasmonic Approach to Enhanced Fluorescence for Applications
587 in Biotechnology and the Life Sciences. *Langmuir* **2012,** *28* (27), 10152-10163.

588 16. Xiong, Y.; Huang, Q.; Canady, T. D.; Barya, P.; Liu, S.; Arogundade, O. H.; Race, C.
589 M.; Che, C.; Wang, X.; Zhou, L. J. N. C., Photonic crystal enhanced fluorescence emission and
590 blinking suppression for single quantum dot digital resolution biosensing. **2022,** *13* (1), 1-14.

591 17. Rissin, D. M.; Kan, C. W.; Campbell, T. G.; Howes, S. C.; Fournier, D. R.; Song, L.;
592 Piech, T.; Patel, P. P.; Chang, L.; Rivnak, A. J.; Ferrell, E. P.; Randall, J. D.; Provuncher, G.
593 K.; Walt, D. R.; Duffy, D. C., Single-molecule enzyme-linked immunosorbent assay detects serum
594 proteins at subfemtomolar concentrations. *Nat Biotechnol* **2010,** *28* (6), 595-599.

595 18. Suo, T.; Liu, X. J.; Feng, J. P.; Guo, M.; Hu, W. J.; Guo, D.; Ullah, H.; Yang, Y.;
596 Zhang, Q. H.; Wang, X.; Sajid, M.; Huang, Z. X.; Deng, L. P.; Chen, T. L.; Liu, F.; Xu, K.;
597 Liu, Y.; Zhang, Q.; Liu, Y. L.; Xiong, Y.; Chen, G. Z.; Lan, K.; Chen, Y., ddPCR: a more
598 accurate tool for SARS-CoV-2 detection in low viral load specimens. *Emerg Microbes Infec* **2020,**
599 *9* (1), 1259-1268.

600 19. Diehl, F.; Li, M.; He, Y. P.; Kinzler, K. W.; Vogelstein, B.; Dressman, D., BEAMing:
601 single-molecule PCR on microparticles in water-in-oil emulsions. *Nat Methods* **2006,** *3* (7), 551-
602 559.

603 20. Poorbaugh, J.; Samanta, T.; Bright, S. W.; Sissons, S. E.; Chang, C. Y.; Oberoi, P.;
604 MacDonald, A. J.; Martin, A. P.; Cox, K. L.; Benschop, R. J., Measurement of IL-21 in human
605 serum and plasma using ultrasensitive MSD S-PLEX (R) and Quanterix SiMoA methodologies. *J*
606 *Immunol Methods* **2019,** *466*, 9-16.

607 21. Kinkhabwala, A.; Yu, Z. F.; Fan, S. H.; Avlasevich, Y.; Mullen, K.; Moerner, W. E.,
608 Large single-molecule fluorescence enhancements produced by a bowtie nanoantenna. *Nat*
609 *Photonics* **2009,** *3* (11), 654-657.

610 22. Khatua, S.; Paulo, P. M. R.; Yuan, H. F.; Gupta, A.; Zijlstra, P.; Orrit, M., Resonant
611 Plasmonic Enhancement of Single-Molecule Fluorescence by Individual Gold Nanorods. *Acs*
612 *Nano* **2014,** *8* (5), 4440-4449.

613 23. Bharadwaj, P.; Anger, P.; Novotny, L., Nanoplasmonic enhancement of single-molecule
614 fluorescence. *Nanotechnology* **2007,** *18* (4).

615 24. Akselrod, G. M.; Argyropoulos, C.; Hoang, T. B.; Ciraci, C.; Fang, C.; Huang, J. N.;
616 Smith, D. R.; Mikkelsen, M. H., Probing the mechanisms of large Purcell enhancement in
617 plasmonic nanoantennas. *Nat Photonics* **2014,** *8* (11), 835-840.

618 25. Hoang, T. B.; Akselrod, G. M.; Argyropoulos, C.; Huang, J. N.; Smith, D. R.; Mikkelsen,
619 M. H., Ultrafast spontaneous emission source using plasmonic nanoantennas. *Nat Commun* **2015,**
620 *6*.

621 26. Liu, J. N.; Huang, Q. L.; Liu, K. K.; Singamaneni, S.; Cunningham, B. T., Nanoantenna-
622 Microcavity Hybrid Resonators with Highly Cooperative Plasmonic-Photonic Coupling. *Ieee*
623 *Photon Conf* **2017**.

624 27. Wang, Z. Y.; Luan, J. Y.; Seth, A.; Liu, L.; You, M. L.; Gupta, P.; Rathi, P.; Wang, Y.
625 X.; Cao, S. S.; Jiang, Q. S.; Zhang, X.; Gupta, R.; Zhou, Q. J.; Morrissey, J. J.; Scheller, E.
626 L.; Rudra, J. S.; Singamaneni, S., Microneedle patch for the ultrasensitive quantification of protein
627 biomarkers in interstitial fluid. *Nat Biomed Eng* **2021,** *5* (1), 64-+.

628 28. Kongsuwan, N.; Demetriadou, A.; Chikkaraddy, R.; Benz, F.; Turek, V. A.; Keyser, U.
629 F.; Baumberg, J. J.; Hess, O., Suppressed Quenching and Strong-Coupling of Purcell-Enhanced
630 Single-Molecule Emission in Plasmonic Nanocavities. *Acs Photonics* **2018,** *5* (1), 186-191.

631 29. Bogdanov, S. I.; Shalaginov, M. Y.; Lagutchev, A. S.; Chiang, C. C.; Shah, D.; Baburin,
632 A. S.; Ryzhikov, I. A.; Rodionov, I. A.; Kildishev, A. V.; Boltasseva, A.; Shalaev, V. M.,
633 Ultrabright Room-Temperature Sub-Nanosecond Emission from Single Nitrogen-Vacancy
634 Centers Coupled to Nanopatch Antennas. *Nano Lett* **2018,** *18* (8), 4837-4844.

635 30. Huang, Q. L.; Cunningham, B. T., Microcavity-Mediated Spectrally Tunable
636 Amplification of Absorption in Plasmonic Nanoantennas. *Nano Lett* **2019,** *19* (8), 5297-5303.

637 31. Heylman, K. D.; Thakkar, N.; Horak, E. H.; Quillin, S. C.; Cherqui, C.; Knapper, K. A.;
638 Masiello, D. J.; Goldsmith, R. H., Optical microresonators as single-particle absorption
639 spectrometers. *Nat Photonics* **2016,** *10* (12), 788-+.

640 32. Huang, Q. L.; Canady, T. D.; Gupta, R.; Li, N. T.; Singamaneni, S.; Cunningham, B. T.,
641 Enhanced Plasmonic Photocatalysis through Synergistic Plasmonic- Photonic Hybridization. *Acs*
642 *Photonics* **2020,** *7* (8), 1994-2001.

643 33. Boroditsky, M.; Vrijen, R.; Krauss, T. F.; Coccioli, R.; Bhat, R.; Yablonovitch, E.,
644 Spontaneous emission extraction and Purcell enhancement from thin-film 2-D photonic crystals.
645 *J Lightwave Technol* **1999,** *17* (11), 2096-2112.

646 34. Luan, J. Y.; Seth, A.; Gupta, R.; Wang, Z. Y.; Rathi, P.; Cao, S. S.; Derami, H. G.;
647 Tang, R.; Xu, B. G.; Achilefu, S.; Morrissey, J. J.; Singamaneni, S., Ultrabright fluorescent
648 nanoscale labels for the femtomolar detection of analytes with standard bioassays. *Nat Biomed*
649 *Eng* **2020,** *4* (5), 518-530.

650 35. Wang, Z. Y.; Zhou, Q. J.; Seth, A.; Kolla, S.; Luan, J. Y.; Jiang, Q. S.; Rathi, P.; Gupta,
651 P.; Morrissey, J. J.; Naik, R. R.; Singamaneni, S., Plasmonically-enhanced competitive assay for
652 ultrasensitive and multiplexed detection of small molecules. *Biosens Bioelectron* **2022,** *200*.

653 36. Wu, D. L.; Milutinovic, M. D.; Walt, D. R., Single molecule array (Simoa) assay with
654 optimal antibody pairs for cytokine detection in human serum samples. *Analyst* **2015,** *140* (18),
655 6277-6282.

656 37. Li, N. T.; Canady, T. D.; Huang, Q. L.; Wang, X.; Fried, G. A.; Cunningham, B. T.,
657 Photonic resonator interferometric scattering microscopy. *Nat Commun* **2021,** *12* (1).

658 38. Zhen, B.; Chua, S. L.; Lee, J.; Rodriguez, A. W.; Liang, X. D.; Johnson, S. G.;
659 Joannopoulos, J. D.; Soljacic, M.; Shapira, O., Enabling enhanced emission and low-threshold
660 lasing of organic molecules using special Fano resonances of macroscopic photonic crystals. *P*
661 *Natl Acad Sci USA* **2013,** *110* (34), 13711-13716.

662 39. Sabri, L.; Shahabadi, M.; Forooraghi, K.; Ghaffari-Miab, M., Interaction of two guided-
663 mode resonances in an all-dielectric photonic crystal for uniform SERS. *Opt Express* **2020,** *28* (7),
664 10467-10476.

665 40. Shi, L. L.; Shang, J. S.; Liu, Z. Q.; Li, Y. Y.; Fu, G. L.; Liu, X. S.; Pan, P. P.; Luo, H.
666 M.; Liu, G. Q., Ultra-narrow multi-band polarization-insensitive plasmonic perfect absorber for
667 sensing. *Nanotechnology* **2020,** *31* (46).

668 41. Ghosh, A. K.; Duong, T. T.; Mckee, S. P.; Thompson, W. J., N,N'-Disuccinimidyl
669 Carbonate - a Useful Reagent for Alkoxycarbonylation of Amines. *Tetrahedron Lett* **1992,** *33* (20),
670 2781-2784.

671 42. Vignali, D. A., Multiplexed particle-based flow cytometric assays. *J Immunol Methods*
672 **2000,** *243* (1-2), 243-55.

673 43. Wilson, D. H.; Rissin, D. M.; Kan, C. W.; Fournier, D. R.; Piech, T.; Campbell, T. G.;
674 Meyer, R. E.; Fishburn, M. W.; Cabrera, C.; Patel, P. P.; Frew, E.; Chen, Y.; Chang, L.; Ferrell,
675 E. P.; von Einem, V.; McGuigan, W.; Reinhardt, M.; Sayer, H.; Vielsack, C.; Duffy, D. C., The
676 Simoa HD-1 Analyzer: A Novel Fully Automated Digital Immunoassay Analyzer with Single-
677 Molecule Sensitivity and Multiplexing. *J Lab Autom* **2016,** *21* (4), 533-47.

678 44. Tebbe, M.; Kuttner, C.; Mannel, M.; Fery, A.; Chanana, M., Colloidally Stable and
679 Surfactant-Free Protein-Coated Gold Nanorods in Biological Media. *Acs Appl Mater Inter* **2015,**
680 *7* (10), 5984-5991.

681 45. Siefke, T.; Kroker, S.; Pfeiffer, K.; Puffky, O.; Dietrich, K.; Franta, D.; Ohlidal, I.;
682 Szeghalmi, A.; Kley, E. B.; Tunnermann, A., Materials Pushing the Application Limits of Wire

683 Grid Polarizers further into the Deep Ultraviolet Spectral Range. *Adv Opt Mater* **2016,** *4* (11),
684 1780-1786.

685

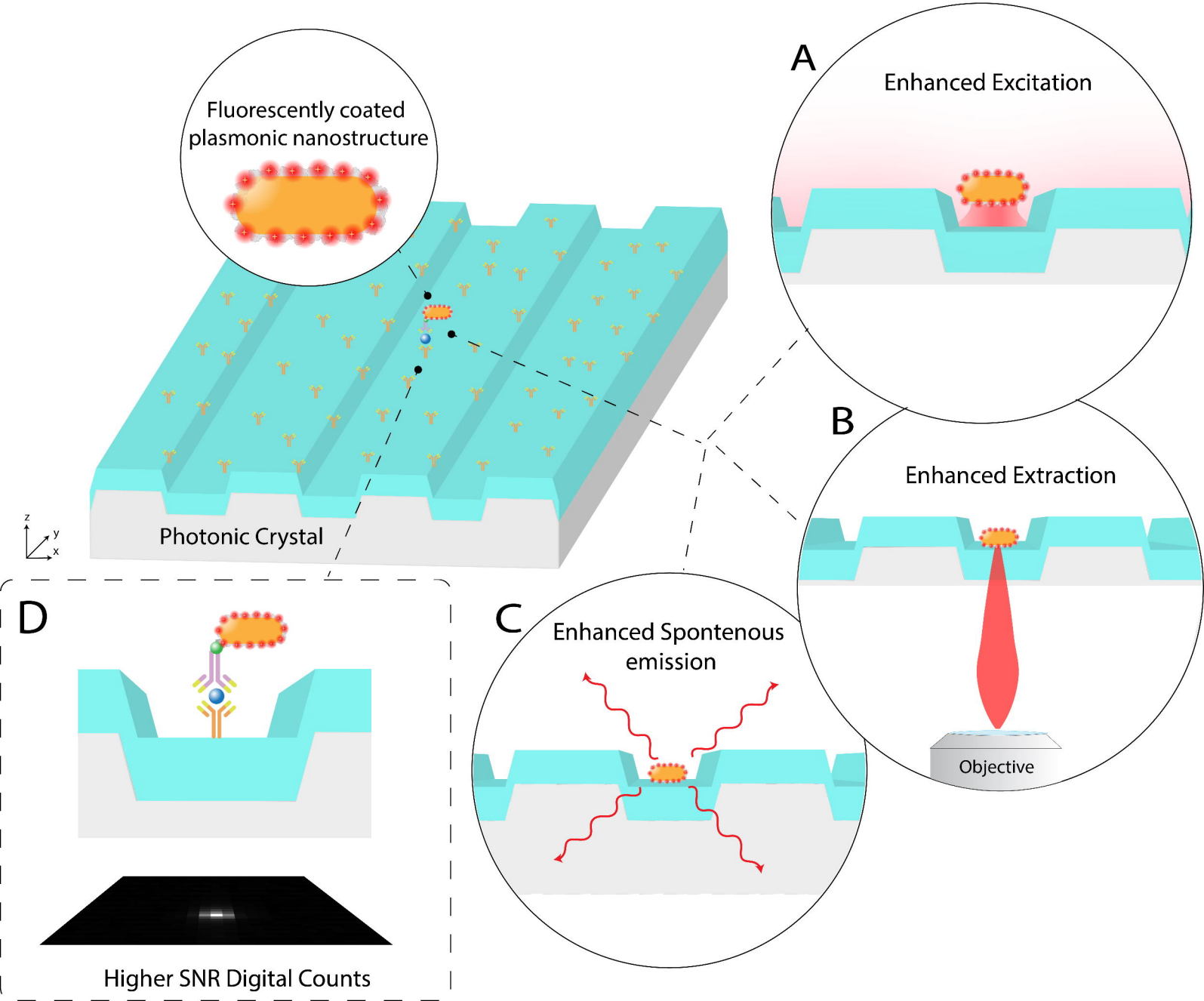
Fluorescently coated plasmonic nanostructure
Photonic Crystal
z
y
x
A
Enhanced Excitation
B
Enhanced Extraction
Objective
C
Enhanced Spontenous emission
D
Higher SNR Digital Counts

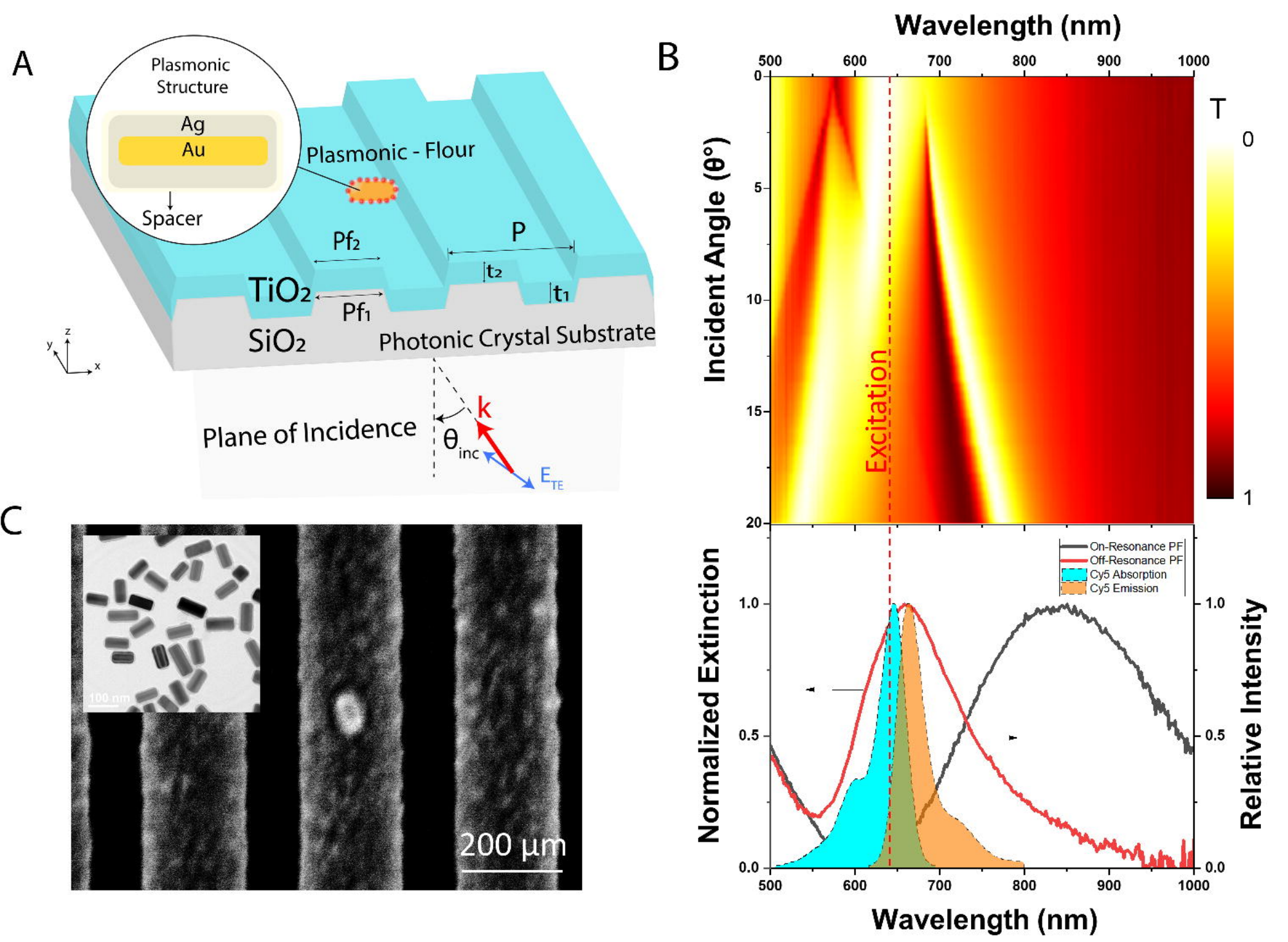
A
Plasmonic Structure
Ag
Au
Spacer
Plasmonic - Flour
Pf2
P
t2
t1
TiO2
Pf1
SiO2
Photonic Crystal Substrate
Plane of Incidence
k
θinc
ETE
B
Wavelength (nm)
Incident Angle (θ°)
Excitation
T
0
1
Normalized Extinction
Relative Intensity
On-Resonance PF
Off-Resonance PF
Cy5 Absorption
Cy5 Emission
Wavelength (nm)
C
100 nm
200 µm

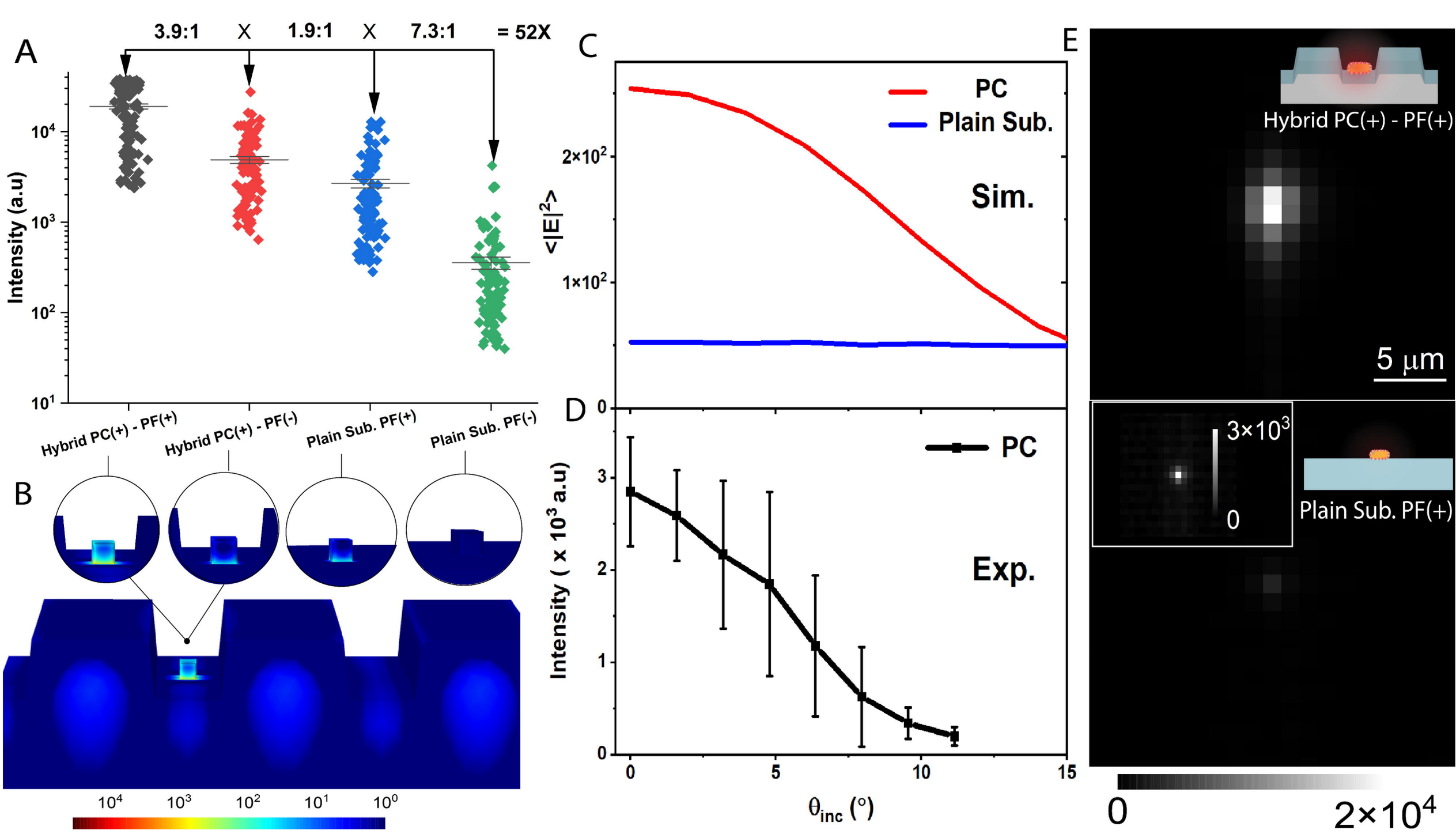
A
3.9:1
X
1.9:1
X
7.3:1
= 52X
Intensity (a.u)
Hybrid PC(+) - PF(+)
Hybrid PC(+) - PF(-)
Plain Sub. PF(+)
Plain Sub. PF(-)
B
C
PC
Plain Sub.
Sim.
<|E|²>
D
PC
Exp.
Intensity (x 10³ a.u)
θinc (°)
E
Hybrid PC(+) - PF(+)
5 μm
3×10³
0
Plain Sub. PF(+)
0
2×10⁴

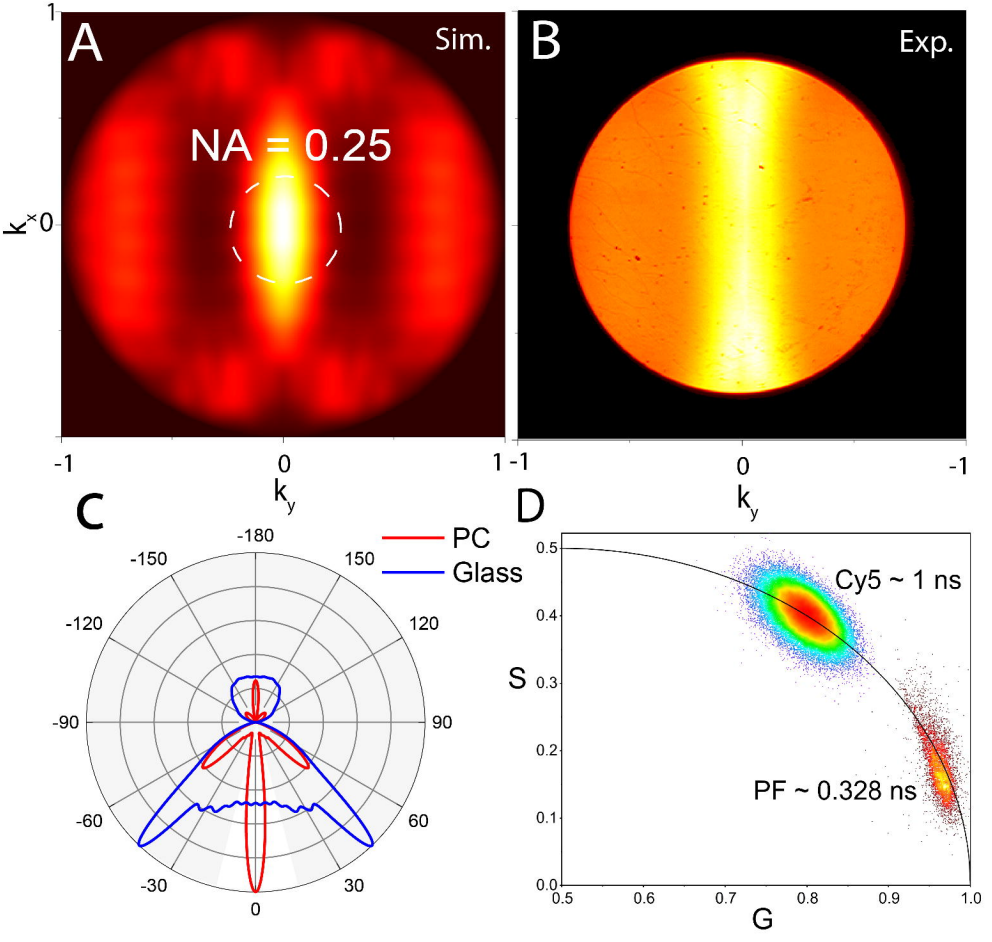
A
Sim.
NA = 0.25
B
Exp.
k_x
k_y
C
PC
Glass
D
Cy5 ~ 1 ns
PF ~ 0.328 ns
S
G

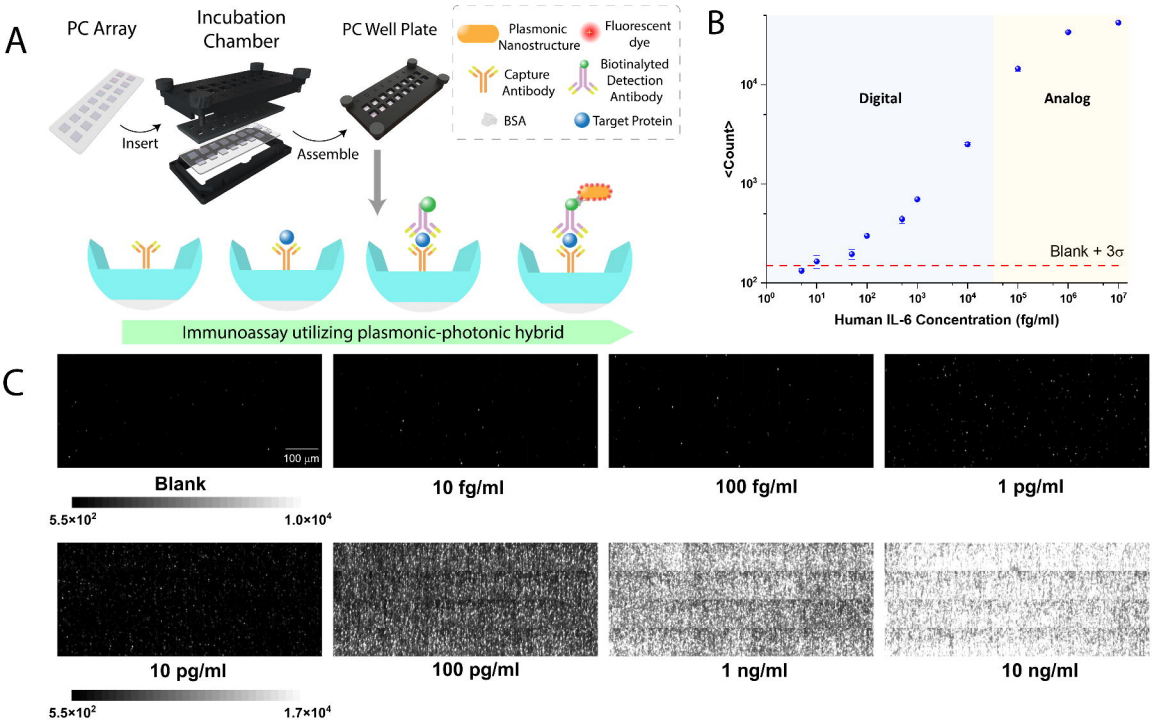
A
PC Array
Incubation Chamber
PC Well Plate
Insert
Assemble
Plasmonic Nanostructure
Fluorescent dye
Capture Antibody
Biotinalyted Detection Antibody
BSA
Target Protein
Immunoassay utilizing plasmonic-photonic hybrid
B
Digital
Analog
Blank + 3σ
<Count>
Human IL-6 Concentration (fg/ml)
C
100 μm
Blank
10 fg/ml
100 fg/ml
1 pg/ml
5.5×10²
1.0×10⁴
10 pg/ml
100 pg/ml
1 ng/ml
10 ng/ml
5.5×10²
1.7×10⁴